Supporting Material

Synergetic Effects of Isoprene and HO_x on Biogenic New Particle Formation

Lee Tiszenkel[1] and Shan-Hu Lee[1,2*]

[1]Department of Atmospheric and Earth Sciences, University of Alabama in Huntsville, Huntsville, Alabama
[2]Department of Chemistry, University of Alabama in Huntsville, Huntsville, Alabama

[*] Corresponding author (shanhu.lee@uah.edu)

Additional methods
Tables S1-S5
Figure S1-S9

Additional methods

A temperature probe (Campbell Scientific CS-215) was used to monitor temperature throughout the experiment. Ozone was generated from the photolysis of oxygen with UV light (with the wavelength of 254 nm, Analytik Jena UVP Pen-Ray). Flows of O_2 and N_2 past the UV light were adjusted to keep a constant O_3 with changing flow conditions in the experiment. In our experiments, OH was generated from ozonolysis of VOCs (hence dark OH source, as opposed to ozone photolysis). Biogenic VOCs (α-pinene and isoprene) react with ozone and OH.

Concentrations of α-pinene and isoprene were measured with GC-FID (gas chromatography with flame ionization detector; Agilent 6890N). VOCs were included in the system by injecting a set volume of liquid α-pinene and isoprene (Fisher Scientific) in to a heated flow of pure N_2 with gas-tight syringes (Hamilton 1700) and syringe pumps (New Era Pump Systems, Just Infusion). A fraction of this heated flow was delivered in to the flow tube. Delivery flow and injection rate of α-pinene were kept constant throughout the experiment. Isoprene (and thus R, ratio of isoprene carbon to monoterpene carbon) was varied by adjusting the injection rate and delivery flow in to the flow tube. Due to the relatively low flow of this heated N_2 in to the system compared to the total flow, temperature in the experiment was not impacted by varying delivery flows.

Each experimental R value was measured for 70 minutes, ensuring stable particle concentrations as well as sufficient particle mass collected on the filter for FIGAERO analysis. Each R value was preceded by 70 minutes of background measurements taken with both the UV light and VOC delivery flows off. The PSM, SMPS and APi-TOF were monitored during background to ensure that the flow tube

was free of particles during these background periods and the flow tube was being flushed with pure N_2. This ensured a clean environment before each experimental trial.

Figure S6 shows the GC-FID measurements for α-pinene and isoprene, using different methods to introduce these biogenic compounds to the flow tube: first using a heated injector from the liquid solution, second using a permeation tube with accurately known concentrations (calibration), and third by introducing these two compounds together with injectors. Although the injector method has been typically used in VOCs experiments, this method uses heated injection lines, so depending on the different temperatures of the injector and the gas line, the produced amount of a specific VOC can vary. As seen in Figure S2, these methods produce consistent amounts of α-pinene and isoprene in the current study. There was a reduction in concentrations of VOCs (α-pinene and isoprene) at the end of the TANGENT compared to those at the beginning, due to wall loss and gas-to-particle conversion. From these measurements we estimated the wall loss of VOCs (Figure S6). We also calculated wall loss of α-pinene using the accommodation coefficient of 0.1 and it was consistent with those obtained from measurements. For isoprene, there was no wall loss.

Possible impurities of ammonia and amines were measured continuously with a CIMS using ethanol as an ion reagent [*You et al.*, 2014; *Huan Yu and Lee*, 2012]. Ammonia and amines are common impurities that originated from deionized water [*Erupe et al.*, 2011; *H. Yu et al.*, 2012]. The CLOUD experiments have shown that positive ion clusters always contain α-pinene and ammonia together [*Frege et al.*, 2018; *Kirkby et al.*, 2016], indicating that base compounds likely contribute to biogenic nucleation. As shown in Figure S7, ammonia and amines were lower than the CIMS detection limits, and their mass spectra signals also decreased with time.

In our system, OH radicals were generated from α-pinene ozonolysis reactions (as a dark source). We have used two independent methods to calculate OH concentrations. First, OH concentrations were simulated using a chemical box model incorporated with the Master Chemical Mechanisms (MCM v.3.3.1) [*Jenkin et al.*, 2015]. Additionally, OH concentrations were also estimated using the measured α-pinene concentrations and following the equation [*Kiendler-Scharr et al.*, 2009; *McFiggans et al.*, 2019] as shown in Supporting Information. These methods show consistent OH concentrations within the uncertainties of estimation.

$$\frac{d[X]}{dt} = \frac{F}{V} \bullet \left([X]_{in} - [X]_{out}\right) - \left(k_{O_3} \bullet \left[O_3\right] + k_{OH} \bullet [OH]\right) \bullet [X]_{out}$$

where $[X]_{in}$ and $[X]_{out}$ indicate α-pinene concentrations at the beginning and end of the reactor, and k_{O3} and k_{OH} indicate the reaction coefficients of α-pinene with ozone and OH, respectively. The box model

calculated the OH concentration of approximately 4×10^7 cm^{-3} with the α-pinene concentration of 60 ppb, ozone of 3.2 ppm, a temperature of 298 K, and RH of 10%, for example. This OH concentration was consistent with that estimated from Eq. 1. The box model also calculated HO_2 concentrations; the corresponding HO_2 was about 6×10^8 cm^{-3} at the above condition.

In the present study, we used "$P_{HOM} \times RT$" to account for the maximum possible production of highly oxidized molecules (HOMs) under certain precursor concentrations (P_{HOM}) and residence time (*RT*). HOM production rate includes HOM formation from both ozonolysis and OH oxidation reactions:

$$P_{HOM} \times RT = (k_{O3} \times [O_3] \times [\alpha\text{-pinene}] \times Y_{ap\text{-}o3} + k_{OH} \times [OH] \times [\alpha\text{-pinene}] \times Y_{ap\text{-}OH}) \times RT$$

where P_{HOM} is the production rate, and $Y_{ap\text{-}o3}$ and $Y_{ap\text{-}OH}$ are the HOM yields from ozone and OH reactions. Table S4 includes these kinetic parameters.

Thermogram of particle-phase HOMs was obtained when heating the FIGAERO inlet, attached to the iodide CIMS, from room temperature to 200 ºC within 30 minutes. Calibration was done with polyethylene glycols (PEG 5-8) via the atomizer method outlined in [*Ylisirniö et al.*, 2021]. From the "maximum" vaporization temperatures (T_{max}) which appeared during the thermogram, we derived saturation vapor pressures (C*) at room temperature based on the calibration using organic compounds with known saturation pressures (Figure S8a). Our calibration results are compared with [*Ye et al.*, 2019] with similar $Log_{10}C^*$ values (Figure S8b).

We also compared the FIGAERO-measured volatilities with those estimated with the volatility basis set (VBS) [*Donahue et al.*, 2011] (Figure S9). Volatilities were calculated from the chemical formulae of the identified compounds according to the following equation:

$$Log_{10}C_i^* = \left(n_c^0 - n_c^i\right)b_c - n_O^i b_O - 2\left(\frac{n_c^i n_O^i}{n_c^i + n_O^i}\right)b_{CO}$$

Where $b_c = 0.475$, $b_O = 2.3$, $b_{CO} = -0.3$, $n_c^0 = 25$, n_c^i is the number of carbons present in the molecule, and n_O^i is the number of oxygens present in the molecule. These results show that, on average, $Log_{10}C^*$ as determined by our calibrated thermogram was an overestimation of the volatilities of these compound classes. Median $Log_{10}C^*$ for C15 was calculated to be approximately -10, and for C20 -18. This places both compound classes in the ULVOC range, which is consistent with the types of HOMs normally required for pure biogenic new particle formation [*Tröstl et al.*, 2016]. More relevantly to our results, the VBS-calculated $Log_{10}C^*$ of lower-mass (thus low O:C) C20 such as those that appear in the particle-phase at high *R* values is approximately -9, more consistent with our thermograms. This discrepancy can be attributed to instrumental sensitivity of the iodide CIMS with respect to more highly

oxygenated compounds. As shown in [*Riva et al.*, 2019], iodide-CIMS sensitivity towards HOM compounds sharply drops as compounds become more oxygenated. As a result, while these compounds may be detected in trace amounts in our experimental system, it is likely that their abundance was greatly underestimated during thermal desorption due to the iodide reagent. But most importantly, this discrepancy also reinforces our previous analysis that volatilities cannot be simply estimated by the number of C, H, O, and N atoms in the component (which is the basis of the VBS), because different functional groups and isomers can affect the volatilities differently as discussed in the main text.

Aerosol nucleation rates (formation rate of 1.8 nm particles), $J_{1.8}$, were calculated from the measured aerosol size distributions, based on [*Dada et al.*, 2020]:

$$J_{1.8}$$

where S_{wall} is the loss to the wall of particles larger than 1.8 nm, and S_{coag} is the loss of particles larger than 1.8 nm due to coagulation with other particles. The term of $\frac{dN_{>1.8\,nm}}{dt}$ was derived from the measured aerosol size distributions. Here, we assume 1.8 nm is the nucleation critical cluster size, as that is the median diameter in the PSM size bin closest to the critical cluster size after data inversion.

For growth rates ($GR = \frac{dD_p}{dt}$) was determined using the measured size distributions at the end of the flow tube and the residence times of FT-1 and FT-2. Parameters used in *J* and *GR* calculations are included in Table S5.

Condensational sink (CS) in our experimental system arose from loss of particles to the flow tube wall as well as the population of particles present in the flow tube. Wall losses were calculated as 1.4×10^{-3} s^{-1} and typical coagulation sink during experiments was 8.8×10^{-3} s^{-1}, resulting in a condensational sink of approximately 1.2×10^{-2} s^{-1}. This is consistent with a typical condensation sink observed in an urban environment, which exhibit CS on the order of 10^{-2} s^{-1} [Lee et al., 2019].

Uncertainties in the calculation of $J_{1.8}$ and growth rate arose from error propagation of both statistical and systematic errors and run-to-run repeatability. The overall error in size distributions, based on standard error between run-to-run experiments under identical conditions, was 42%. Inter-run systematic error included uncertainty in wall loss (7%), coagulation sink (20%) and sampling losses (10%). Uncertainties in particle diameter from the inversion of the PSM measurement are estimated at approximately 12% (or ±0.2 nm) for particles in the size range observed in this experiment (Lehtipalo et al., 2016). The overall scale uncertainty in $J_{1.8}$ was calculated as 48%. The overall scale uncertainty in GR was calculated as 51%.

Table S1. Typical experimental conditions used in this study and the cited previous studies.

	[α-pinene] (ppb)	**[isoprene] (ppb)**	**R**	**[O_3] (ppb)**	**[OH] (ppt)**	**HOM Oxidant Ratio***
This Study	238	0	0	1200	1.6	1.2×10^{0}
	238	23	0.05	1200	1.3	7.9×10^{0}
	238	97	0.2	1200	0.86	3.1×10^{0}
	238	236	0.5	1200	0.52	2.1×10^{0}
	238	482	1.0	1200	0.36	1.5×10^{0}
	238	1201	2.5	1200	0.2	1.1×10^{0}
	238	2469	5.2	1200	0.11	9.1×10^{-1}
	238	5265	11.1	1200	9.1×10^{-2}	5.4×10^{-1}
	0	5265	-	1200	5.3×10^{-2}	2.7×10^{0}
[*Heinritzi et al.*, 2020]	0.77	0	0	49	41	2.1×10^{-3}
	0.456	0	0	49	41	2.1×10^{-3}
	1.442	0	0	49	41	2.1×10^{-3}
	0.677	2.7	1.9	39	8.2	1.1×10^{-3}
	1.326	2.7	1.0	39	8.2	2.1×10^{-3}
	2.636	2.7	0.5	39	8.2	4.2×10^{-3}
	0.677	4.9	3.6	39	8.2	5.9×10^{-4}
	1.326	4.9	1.9	39	8.2	1.1×10^{-3}
	2.636	4.9	0.9	39	8.2	2.3×10^{-3}
	0.677	9.8	7.2	39	8.2	3.0×10^{-4}
	1.326	9.8	3.7	39	8.2	5.8×10^{-4}
	2.636	9.8	1.9	39	8.2	1.1×10^{-3}
[*Wang et al.*, 2021]	30	0	0	3500	1.6	3.7×10^{0}
	30	30	0.5	3500	0.52	6.1×10^{0}
	30	60	1	3500	0.37	4.3×10^{0}
	30	90	1.5	3500	0.29	3.6×10^{0}
	30	120	2	3500	0.24	3.3×10^{0}

*HOM oxidant ratio was calculated as the ratio of ozonolysis to OH oxidation, calculated by dividing the HOM production from ozonolysis of α-pinene by the HOM production from OH reacting with isoprene. Values >1 indicate an ozone dominant oxidation scheme, while values <1 indicate OH dominance.

Table S2. Top-20 ion peaks identified in the gas phase from the present study.

Pure α-pinene	**R = 0.2**	**R = 1.1**	**R = 5.2**	**R = 11.1**
C9H14IO4	C9H14IO4	C5H10IO3	C5H10IO3	C2H4IO4
C10H16IO6	C5H10IO3	C8H12IO5	C2H4IO4	C5H10IO3
C10H16IO3	C10H16IO6	C9H14IO4	C7H8IO5	CH2IO2
C10H16IO4	C8H12IO5	C10H16IO3	C3H4IO5	CH2IO4
C8H12IO5	C10H16IO3	C8H12IO4	C7H8IO6	C3H4IO5
C8H12IO4	C10H16IO4	C10H16IO4	C8H10IO5	C7H8IO5
C10H16IO5	C8H12IO4	C10H16IO6	C4H6IO5	C4H6IO5
C9H14IO5	C9H14IO5	C9H14IO5	C9H13O4	C2H4IO5
C7H8IO4	C10H16IO5	C5H10IO6	C7H6IO5	C5H8IO4
C7H10IO4	C7H10IO4	C2H4IO4	CH2IO4	C5H8IO6
C7H10IO5	C7H8IO4	C7H10IO4	C8H11O4	C2H4IO7
C11H22IO2	C5H10IO6	C7H8IO4	C6H6IO5	C3H2IO4
C9H14IO6	C7H10IO5	C10H16IO5	C3H3IO5	C3H3IO5
C8H10IO4	C8H10IO4	C8H10IO4	C3H2IO4	CH2IO5
C9H14IO3	C9H14IO6	C7H10IO5	C5H8IO6	C8H10IO5
C5H10IO3	C9H13O4	C9H14IO6	C3H4IO4	C7H8IO6
C8H12IO3	C9H14IO3	C9H13O4	C5H8IO2	C7H6IO5
C10H16IO7	CH2IO2	CH2IO2	C6H6IO6	C4H4IO6
C3H4IO4	C11H22IO2	C9H14IO3	C8H10IO6	C5H8IO2
C9H13O4	C10H16IO7	C5H10IO4	C4H4IO4	C3H4IO4

Table S3. Top-20 ion peaks identified in the particle phase from the present study.

Pure α-pinene	**R = 0.2**	**R = 1.1**	**R = 5.2**	**R = 11.1**
C8H12IO4	C8H12IO4	C8H12IO4	C8H12IO4	C8H12IO4
C9H14IO4	C9H14IO4	C9H14IO4	C9H14IO4	C9H14IO4
C12H12IO	C12H12IO	C12H12IO	C12H12IO	C12H12IO
C7H10IO4	C7H10IO4	C7H10IO4	C7H10IO4	C10H16IO4
C10H16IO4	C10H16IO3	C9H14IO5	C5H10IO3	C7H10IO4
C8H10IO4	C10H16IO4	C8H10IO4	C10H16IO3	C5H10IO3
C9H14IO5	C9H14IO5	C10H16IO4	C9H14IO5	C10H16IO6
C10H16IO3	C8H10IO4	C10H16IO3	C10H16IO4	C9H14IO5
C7H8IO4	C7H8IO4	C7H8IO4	C8H10IO4	C10H16IO5
C10H16IO5	C5H10IO3	C10H20IO2	C7H8IO4	C8H10IO4
C8H12IO5	C9H14IO3	C5H10IO3	C10H20IO2	C9H14IO6
C8H12IO3	CH2IO2	CH2IO2	CH2IO2	C10H16IO3
C9H14IO3	C10H20IO2	C10H16IO5	C9H14IO3	C10H14IO5
C7H12IO4	C8H12IO5	C9H14IO3	C10H16IO5	C10H20IO2
C8H14IO3	C10H16IO5	C8H12IO5	C8H12IO5	C15H18IO5
C10H14IO4	C8H12IO3	C11H22IO2	C10H16IO6	CH2IO2
C11H22IO2	C11H22IO2	C8H12IO3	C10H14IO5	C8H12IO5
C10H20IO2	C3H4IO4	C5H8IO4	C11H22IO2	C10H16IO7
C10H16IO6	C5H8IO4	C3H4IO4	C8H12IO3	C7H8IO4
CH2IO2	C8H14IO3	C8H14IO3	C5H8IO4	C9H14IO3

Table S4. Kinetics parameters used in the calculation of P_{HOM}.

Y_{HOM*O_3}	2.9%	*[Kirkby et al., 2016]*
Y_{HOM*OH}	1.2%	*[Kirkby et al., 2016]*
k_{MT*O_3}	$8.05 \times 10^{-16} \exp exp\left(-\frac{640}{T}\right)$	*[Atkinson et al., 2006]*
k_{MT*OH}	$1.2 \times 10^{-11} \exp exp\left(\frac{440}{T}\right)$	*[Atkinson et al., 2006]*

Table S5. Parameters used in the calculation of *J* and *GR*.

$D_{\alpha\text{-pinene}}$	0.0716	*[Tang et al., 2015]*
λ	0.0651	*[Seinfeld and Pandis, 2016]*
α-pinene accommodation coefficient (α)	0.1	*[Davidovits et al., 2006]*
$k_{wall,\text{FT-1}}$	1.1×10^{-3}	Calculated based on [*Young et al.*, 2008]
$k_{wall,\text{FT-2}}$	6.5×10^{-4}	Calculated based on [*Young et al.*, 2008]

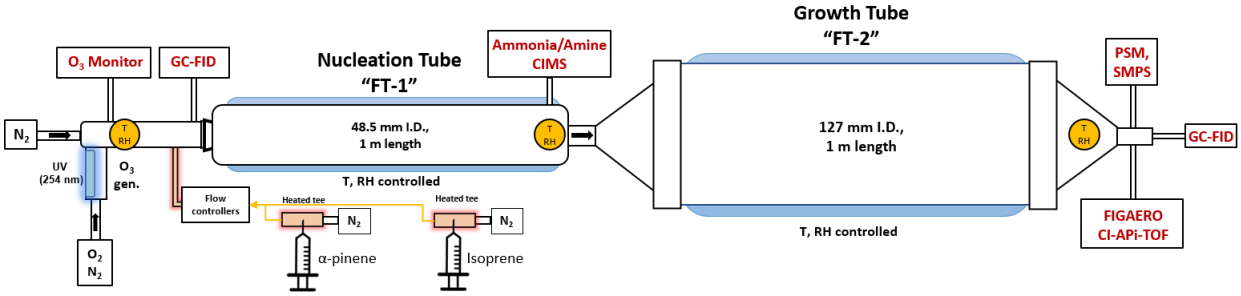

Figure S1. Schematic diagram of the TANGENT (Tandem Aerosol Nucleation and Growth Environment Tube) [*Tiszenkel et al.*, 2019] experimental setup used in this study for biogenic NPF studies. PSM, particle size magnifier. In TAGENT, nucleation takes place in FT-1, and the subsequent growth of nucleated clusters takes place in FT-2, so we can control nucleation and growth under separate environments. But in the present study, FT-1 and FT-2 were kept the same experimental conditions. Experiments were conducted at room temperature at dry conditions (RH lower than 10%). The residence times were typically around 150 s.

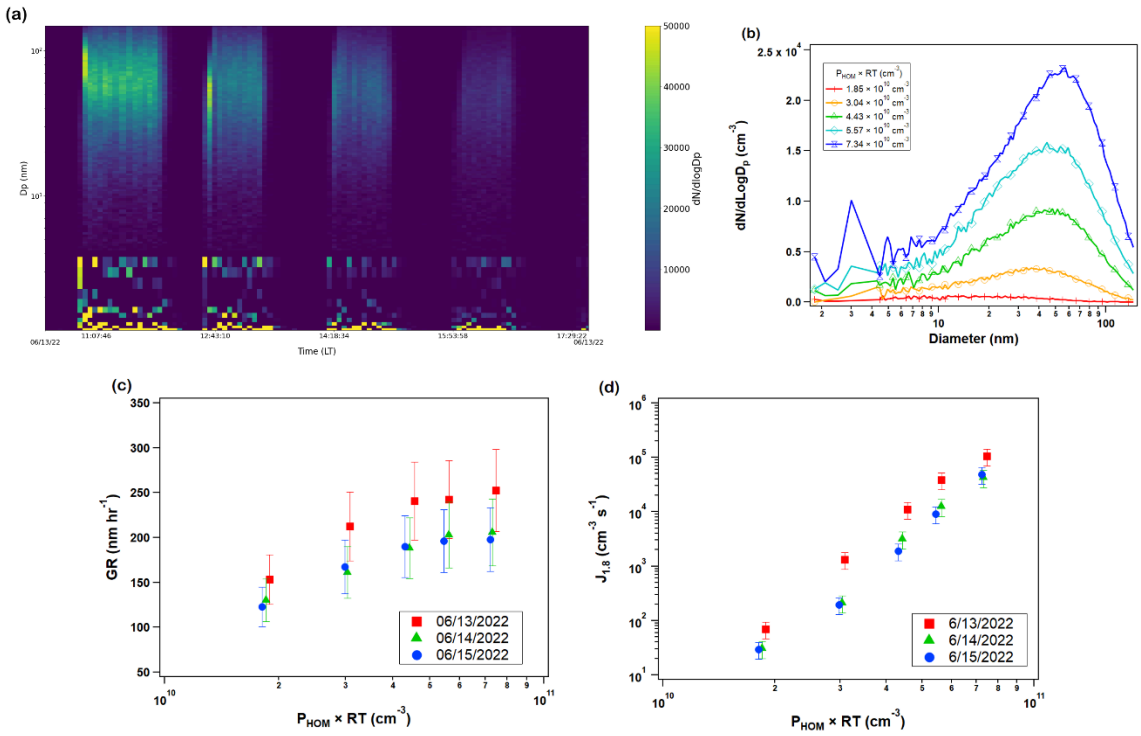

Figure S2. An example of the evolution of aerosol sizes and number concentrations for one specific day are shown. The data shown here are from experiments of particles formed from α-pinene ozonolysis under varying ozone concentrations. α-pinene was held at a constant 60 ppb. Ozone ranged from 442 to 1747 ppb (a) Average size distributions of aerosols measured under the same conditions over three days (b), along with the corresponding growth rates (c) and nucleation rates (d), are shown.

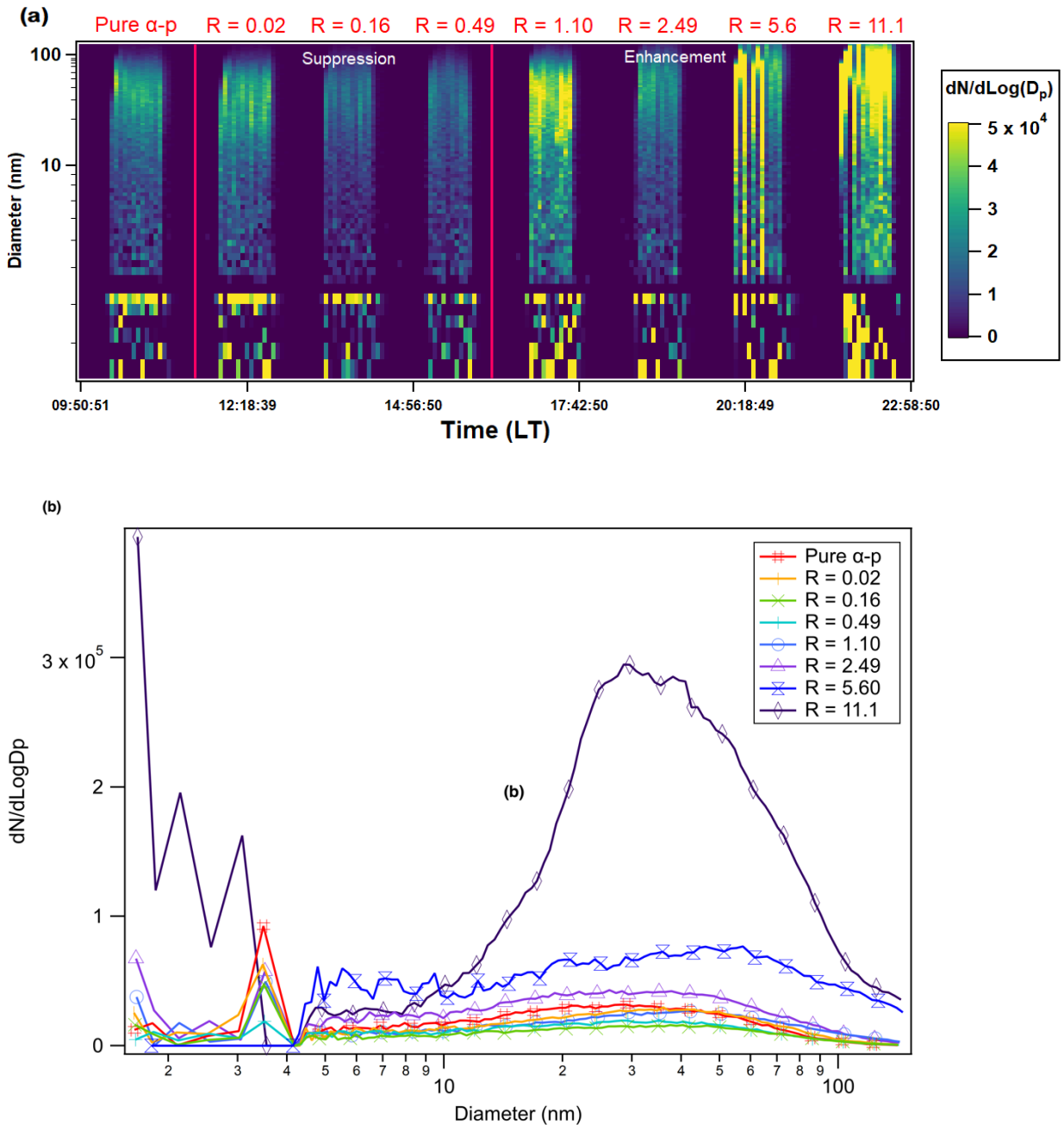

Figure S3. Time series (a) and average size distributions for each trial (b) of an experimental run. Concentrations of α-pinene and ozone were held at a constant 238 ppb and 1200 ppb, respectively. Isoprene was varied from 23.9 ppb to 5265.8 ppb, resulting in a span of *R* (ratio of isoprene carbon to monoterpene carbon) from 0.02 to 11.1.

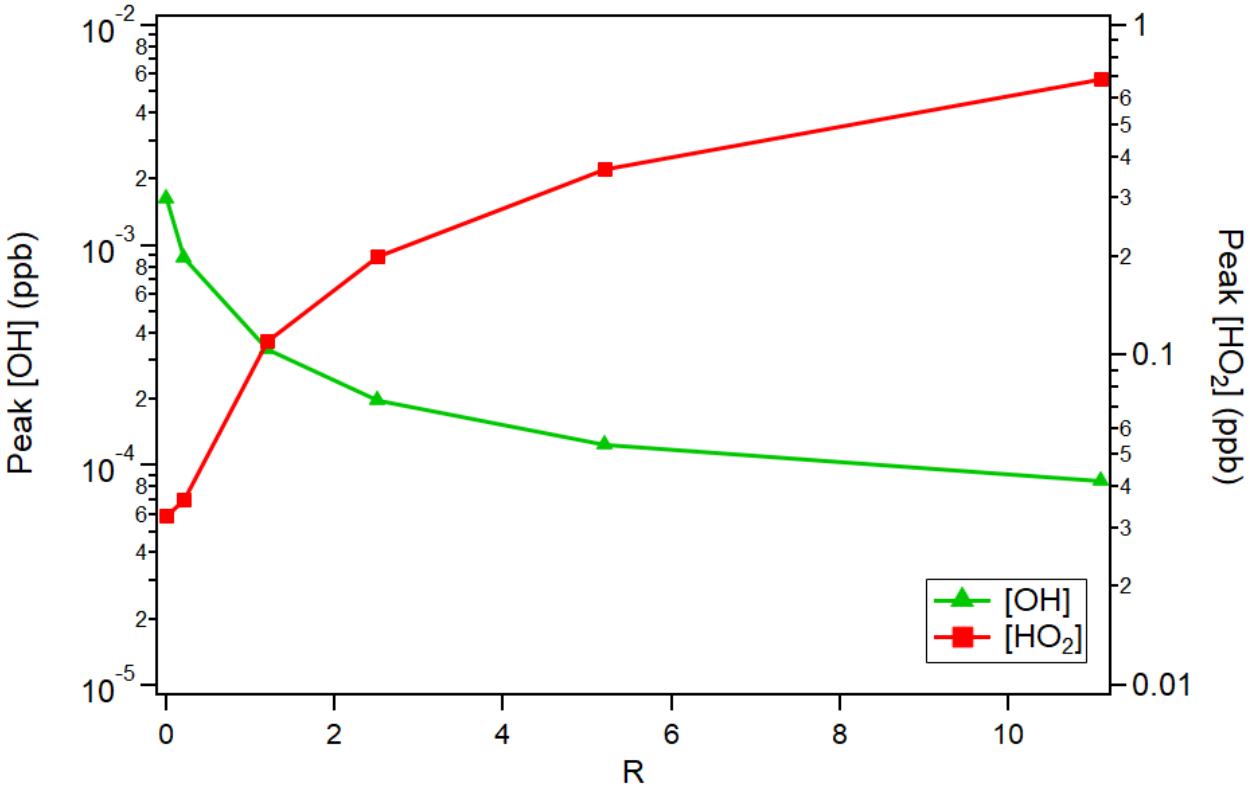

Figure S4. Box model simulation of the maximum OH and HO_2 concentrations present under different R conditions (the same experimental conditions as in Figure 1). The box model was incorporated with the Master Chemical Mechanism (MCM) v.3.3.1 [*Jenkin et al.*, 2015]. The lines connect data points to guide the eye.

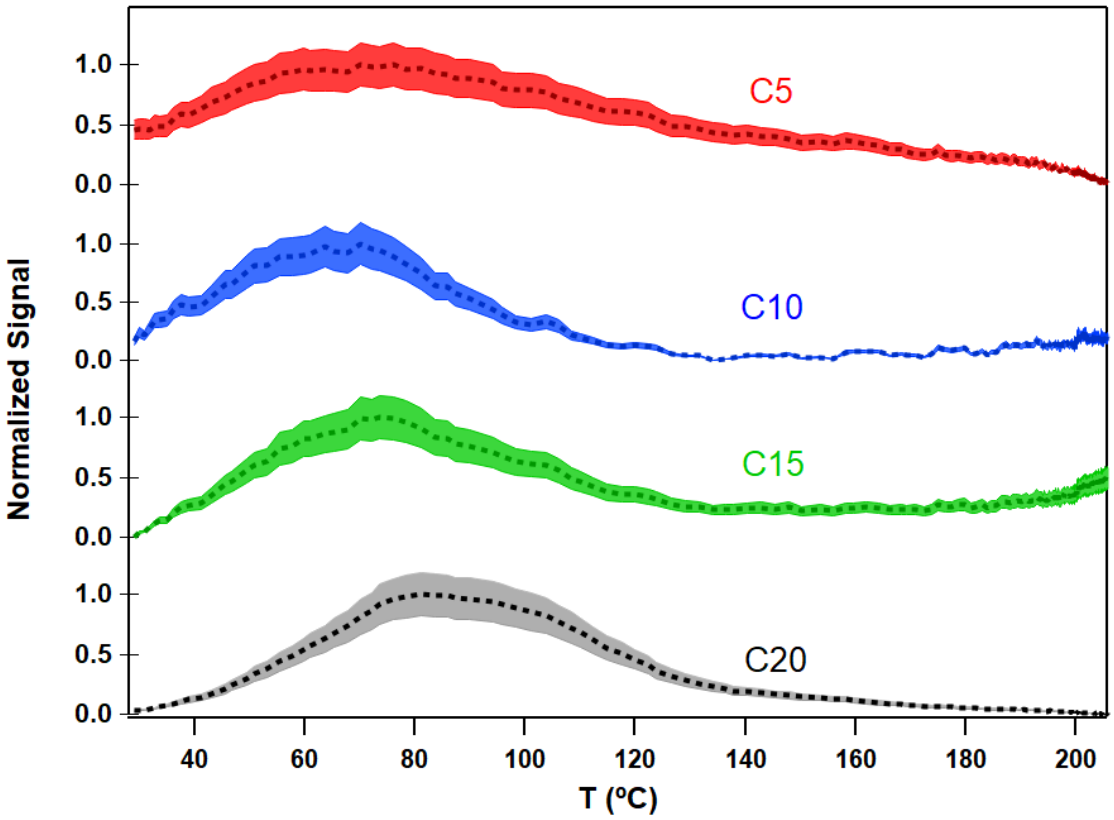

Figure S5. The average temperature-programmed desorption profiles of HOMs for C5 (C5 only), C10 (C6-10), C15 (C11-15), and C20 (C16-20) groups over a 30-minute FIGAERO heating program. Shaded areas indicate one sigma deviation across desorption trials.

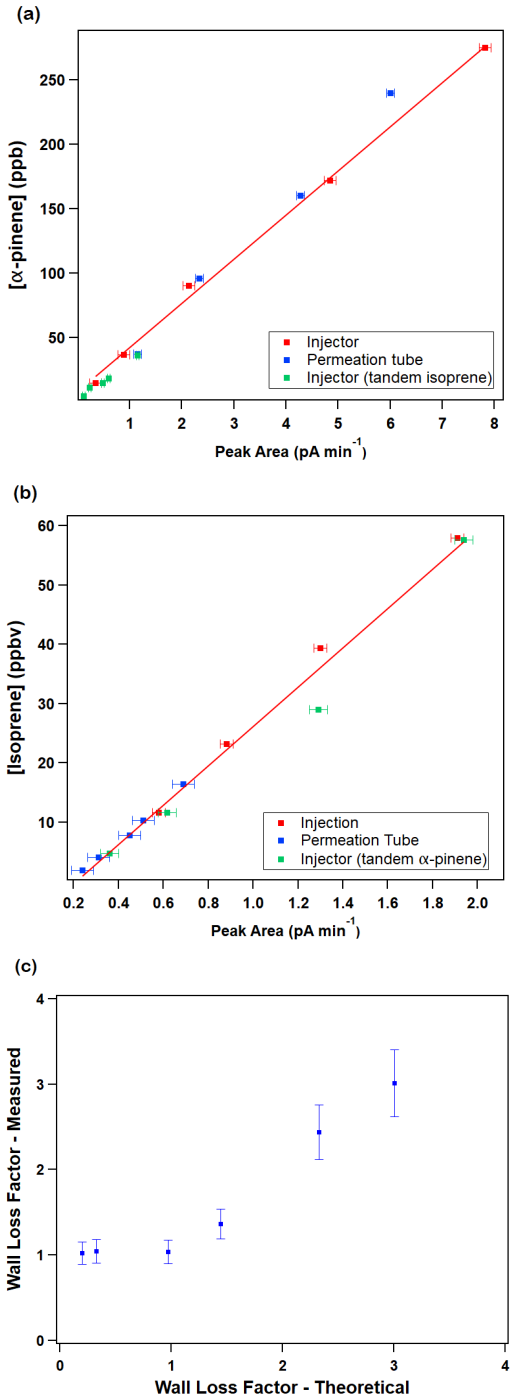

Figure S6. GC-FID calibration for α-pinene (a) and isoprene (b). Three different methods are used to introduce isoprene and α-pinene, first using an injector (a conventional method used in VOCs experiments), second using a permeation tube (calibration), and third injecting these two compounds together (to see potential matrix effects in GC-FID detection). (c) Wall loss characterization of α-pinene with GC-FID, compared with predicted wall loss factors calculated assuming the diffusion-limited

process using accommodation coefficient of α-pinene of 0.1. On the other hand, there was no wall loss for isoprene.

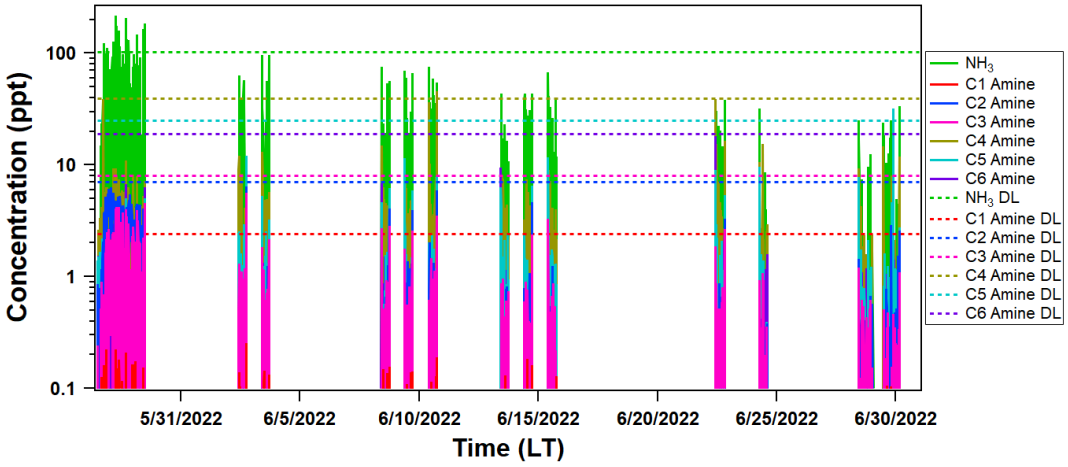

Figure S7. An example of the CIMS measurements for ammonia and C1-C6 amines. The detection limits (defined as three times of the standard deviation of the background values) of these reduced nitrogen compounds are also shown.

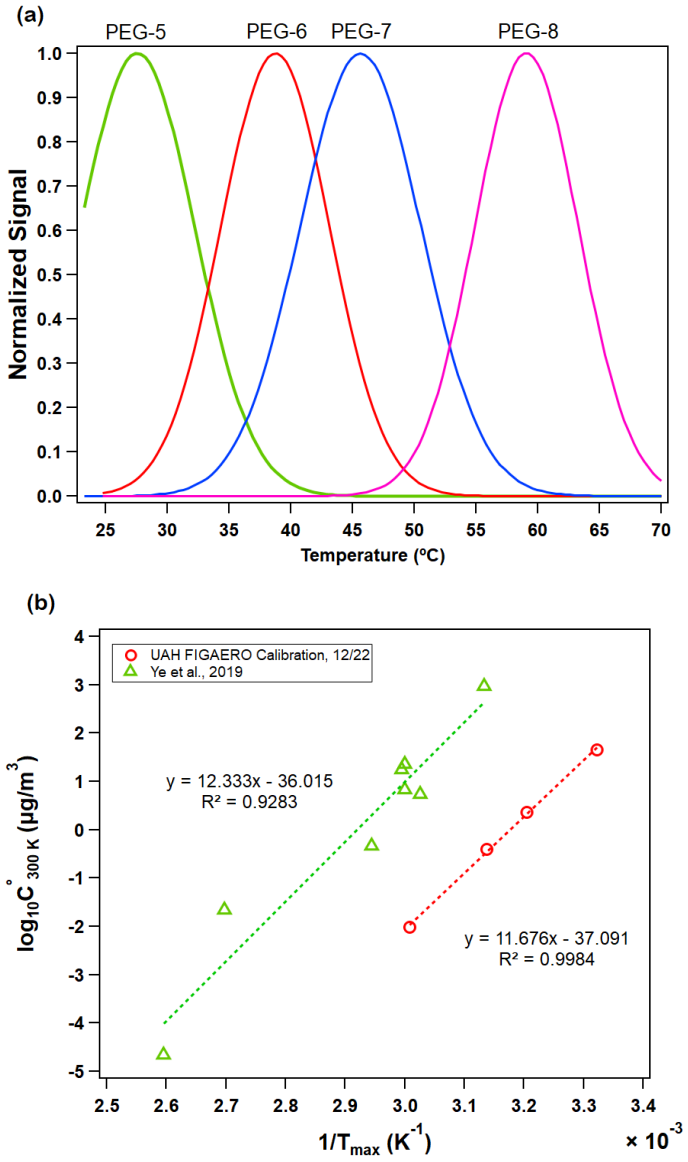

Figure S8. Calibration of FIGAERO thermogram. (a) Gaussian fit and normalized thermogram signals for each PEG desorption cycle. (b) Calibration curve as a result of FIGAERO calibration. The results are presented with a comparison to calibration with similar $Log_{10}C^*$ values shown in [*Ye et al.*, 2019].

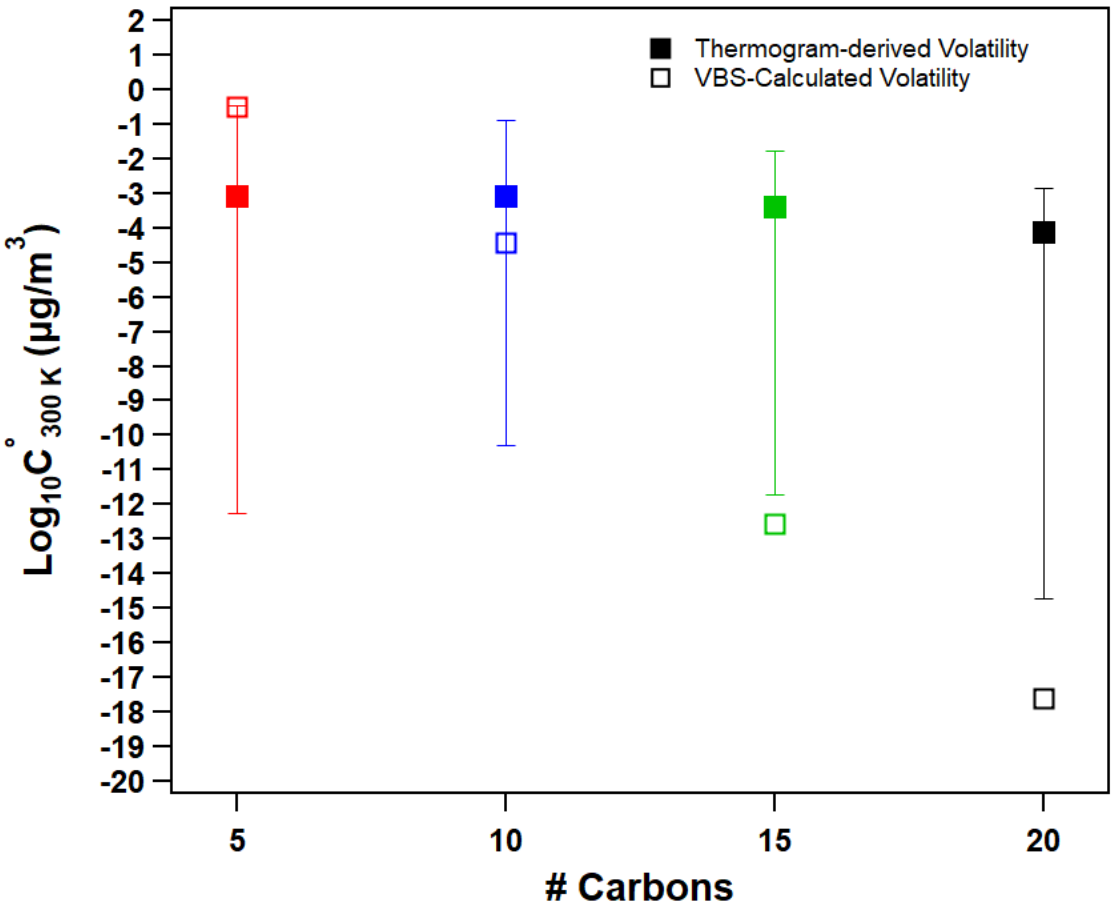

Figure S9. Thermogram derived and VBS calculated volatilities for each class of HOM observed during this study.

References:

Atkinson, R., D. L. Baulch, R. A. Cox, J. N. Crowley, R. F. Hampson, R. G. Hynes, M. E. Jenkin, M. J. Rossi, J. Troe, and I. Subcommittee (2006), Evaluated kinetic and photochemical data for atmospheric chemistry: Volume II – gas phase reactions of organic species, *Atmos. Chem. Phys.*, *6*(11), 3625-4055, doi:10.5194/acp-6-3625-2006.

Dada, L., et al. (2020), Formation and growth of sub-3-nm aerosol particles in experimental chambers, *Nature Protocols*, *15*(3), 1013-1040, doi:10.1038/s41596-019-0274-z.

Davidovits, P., C. E. Kolb, L. R. Williams, J. T. Jayne, and D. R. Worsnop (2006), Mass Accommodation and Chemical Reactions at Gas−Liquid Interfaces, *Chemical Reviews*, *106*(4), 1323-1354, doi:10.1021/cr040366k.

Donahue, N. M., S. A. Epstein, S. N. Pandis, and A. L. Robinson (2011), A two-dimensional volatility basis set: 1. Organic-aerosol mixing thermodynamics, *Atmos. Chem. Phys.*, *11*, 3303-3318, doi:Doi: 10.5194/acp-11-3303-2011.

Erupe, M. E., A. A. Viggiano, and S. H. Lee (2011), The effect of trimethylamine on atmospheric nucleation involving H_2SO_4, *Atmos. Chem. Phys.*, *11*, 4767-4775.

Frege, C., et al. (2018), Influence of temperature on the molecular composition of ions and charged clusters during pure biogenic nucleation, *Atmos. Chem. Phys.*, *18*(1), 65-79, doi:Doi: 10.5194/acp-18-65-2018.

Heinritzi, M., et al. (2020), Molecular understanding of the suppression of new-particle formation by isoprene, *Atmos. Chem. Phys.* , *20*, 11809–11821, doi:10.5194/acp-2020-51.

Jenkin, M. E., J. C. Young, and A. R. Rickard (2015), The MCM v3.3.1 degradation scheme for isoprene, *Atmos. Chem. Phys.*, *15*(20), 11433-11459, doi:10.5194/acp-15-11433-2015.

Kiendler-Scharr, A., J. Wildt, M. Dal Maso, T. Hohaus, E. Kleist, T. F. Mente, R. Tillmann, R. Uerlings, U. Schurr, and A. Wahner (2009), New particle formation in forests inhibited by isoprene emissions, *Nature*, *461*, 381-384.

Kirkby, J., et al. (2016), Ion-induced nucleation of pure biogenic particles, *Nature*, *533*(7604), 521-526, doi:Doi: 10.1038/nature17953.

McFiggans, G., et al. (2019), Secondary organic aerosol reduced by mixture of atmospheric vapours, *Nature*, *565*(7741), 587-593, doi:10.1038/s41586-018-0871-y.

Riva, M., et al. (2019), Chemical transformations in monoterpene-derived organic aerosol enhanced by inorganic composition, *npj Climate and Atmospheric Science*, *2*(1), 2, doi:10.1038/s41612-018-0058-0.

Seinfeld, J. H., and S. N. Pandis (2016), *Atmospheric chemistry and physics: from air pollution to climate change*, John Wiley and Sons, Inc., New Jersey.

Tang, M. J., M. Shiraiwa, U. Pöschl, R. A. Cox, and M. Kalberer (2015), Compilation and evaluation of gas phase diffusion coefficients of reactive trace gases in the atmosphere: Volume 2. Diffusivities of organic compounds, pressure-normalised mean free paths, and average Knudsen numbers for gas uptake calculations, *Atmos. Chem. Phys.*, *15*(10), 5585-5598, doi:10.5194/acp-15-5585-2015.

Tiszenkel, L., C. Stangl, J. Krasnomowitz, Q. Ouyang, H. Yu, M. J. Apsokardu, M. V. Johnston, and S. H. Lee (2019), Temperature effects on sulfuric acid aerosol nucleation and growth: initial results from the TANGENT study, *Atmos. Chem. Phys.*, *19*(13), 8915-8929, doi:10.5194/acp-19-8915-2019.

Tröstl, J., et al. (2016), The role of low-volatility organic compounds in initial particle growth in the atmosphere, *Nature*, *533*(7604), 527-531, doi:Doi: 10.1038/nature18271.

Wang, Y., Y. Zhao, Z. Li, C. Li, N. Yan, and H. Xiao (2021), Importance of Hydroxyl Radical Chemistry in Isoprene Suppression of Particle Formation from α-Pinene Ozonolysis, *ACS Earth and Space Chemistry*, *5*(3), 487-499, doi:10.1021/acsearthspacechem.0c00294.

Ye, Q., et al. (2019), Molecular Composition and Volatility of Nucleated Particles from α-Pinene Oxidation between −50 °C and +25 °C, *Environmental Science & Technology*, *53*(21), 12357-12365, doi:10.1021/acs.est.9b03265.

Ylisirniö, A., L. M. F. Barreira, I. Pullinen, A. Buchholz, J. Jayne, J. E. Krechmer, D. R. Worsnop, A. Virtanen, and S. Schobesberger (2021), On the calibration of FIGAERO-ToF-CIMS: importance and impact of calibrant delivery for the particle-phase calibration, *Atmos. Meas. Tech.*, *14*(1), 355-367, doi:10.5194/amt-14-355-2021.

You, Y., et al. (2014), Atmospheric amines and ammonia measured with a Chemical Ionization Mass Spectrometer (CIMS), *Atmos. Chem. Phys.* , *14*, 12181-12194, doi:Doi: 10.5194/acpd-14-16411-2014.

Young, L. H., D. R. Benson, F. Rifkha, J. R. Pierce, H. Junninen, M. Kulmala, and S. H. Lee (2008), Laboratory studies of sulfuric acid and water binary homogeneous nucleation: evaluation of laboratory setup and preliminary results, *Atmos. Chem. Phys.*, *8*, 1-20.

Yu, H., and S.-H. Lee (2012), Chemical ionisation mass spectrometry for the measurement of atmospheric amines, *Environ. Chem.*, *9*(3), 190-201.

Yu, H., R. McGraw, and S. H. Lee (2012), Effects of amines on formation of sub-3 nm particles and their subsequent growth, *Geophys. Res. Lett.*, *39*, Doi: 10.1029/2011gl050099, doi:10.1029/2011gl050099.